Original article

Relaxation oscillations in a nearly inviscid Faraday system

María Higuera , Edgar Knobloch , José M. Vega

E.T.S.I. Aeronáuticos, Universidad Politécnica de Madrid, Plaza Cardenal Cisneros 3, 28040 Madrid, Spain
Department of Applied Mathematics, University of Leeds, Leeds LS2 9JT, UK
Department of Physics, University of California, Berkeley, CA 94720, USA

Abstract. In the nearly inviscid regime parametrically driven surface gravity-capillary waves couple to a streaming flow driven in oscillatory viscous boundary layers. In an elliptical container of small eccentricity this coupling can lead to relaxation oscillations.

Key words: Faraday oscillations, forced symmetry breaking, global bifurcations, relaxation oscillations

1 Introduction

In recent work on parametrically driven Faraday waves we have shown that in the presence of small viscosity ($C_g \equiv \nu(gh^3 + Th/\rho)^{-1/2} \ll 1$) the waves couple to a streaming flow driven in oscillatory viscous boundary layers at rigid walls and the free surface [12]. This flow in turn affects the waves responsible for the oscillatory boundary layers. While a detailed description of this feedback loop (and the derivation of the asymptotically exact equations) is very involved, it is known [9, 12] that this coupling is responsible for different types of drift instabilities of the waves, instabilities that have been observed in experiments in annular containers [2] but are absent from the theory when the coupling to the streaming flow is neglected.

These instabilities arise not only in annular containers but in cylindrical containers as well, and are driven by a coupling between the streaming flow and the spatial phase of the waves. Richer dynamics result when the container is deformed into an elliptical one. This case is interesting even in the absence of a streaming flow because it results in competition between two nearly degenerate standing waves. As shown in [7] in this case the streaming flow also couples to the *amplitudes* of the standing waves, resulting in a much stronger coupling between the waves and the streaming flow. In this paper we explore the consequences of this coupling in model equations derived in [7] under the assumption that the Reynolds number of the streaming flow is small:

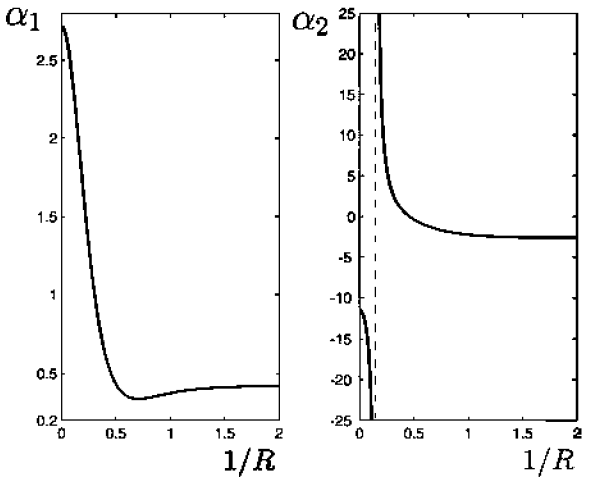

Fig. 1. The coefficients α_1, α_2 for an $m = 1$ inviscid mode with a free contact line as a function of the aspect ratio R. Here $\alpha_1 = -A - B$, $\alpha_2 = -A + B$, where A and B are computed by Miles [10]

$$X' = -(1 + i(\Gamma + \Lambda))X + i\big((\alpha_1 + \alpha_2)|X|^2 + 2\alpha_1|Y|^2\big)X - i(\alpha_1 - \alpha_2)\overline{X}Y^2 + i\mu\overline{X} - 2\gamma v Y, \tag{1}$$

$$Y' = -(1 + i(\Gamma - \Lambda))Y + i\big((\alpha_1 + \alpha_2)|Y|^2 + 2\alpha_1|X|^2\big)Y - i(\alpha_1 - \alpha_2)\overline{Y}X^2 + i\mu\overline{Y} + 2\gamma v X, \tag{2}$$

$$v' = \varepsilon\big(-v + i(\overline{X}Y - X\overline{Y})\big). \tag{3}$$

Here X and Y are the (complex) amplitudes of Faraday waves oriented along the two axes of the ellipse, while v is a real variable proportional to the amplitude of the large scale (axisymmetric and purely azimuthal) component of the streaming flow. In these equations time has been scaled relative to the viscous damping time. In the following we assume that v is weakly damped ($\varepsilon \ll 1$), and use the coefficients α_1, α_2 computed by Miles [10] for a right circular cylinder with a moving contact line boundary condition, viz. $\alpha_1 = 0.4$, $\alpha_2 = -2.58$ for a cylinder of height $h = 14.1$ cm and radius $Rh = 9.2$ cm (Fig. 1). The coefficients μ, Γ, and Λ are proportional to the forcing amplitude, detuning, and eccentricity of the container, respectively, while γ measures the coupling to the streaming flow. For a pinned contact line the first two coefficients are known [8]; γ remains to be computed. In the following we take $\Gamma = -0.5$, $\Lambda = 0.4$, $\gamma = -0.6$, $\varepsilon = 0.01$, and examine the properties of these equations as μ increases.

Equations (1)–(3) are equivariant with respect to the group D_2 generated by the two reflections

$$R_1 \ : \ (X, Y, v) \to (-X, Y, -v), \qquad R_2 \ : \ (X, Y, v) \to (X, -Y, -v). \tag{4}$$

As a result there are two types of steady states, the *Pure Modes* ($P_\pm$) given by $P_+ \equiv (0, Y, 0) = (0, R_+ e^{i\phi_+}, 0)$ and $P_- \equiv (X, 0, 0) = (R_- e^{i\phi_-}, 0, 0)$, with P_+ invariant under R_1 and P_- under R_2, and the *Mixed Modes* (M) given by $M \equiv (X, Y, v) = (R_- e^{i\phi_-}, R_+ e^{i\phi_+}, v)$. Both are shown in Fig. 2 together with their stability properties. Note that both pure mode branches bifurcate subcritically. The P_- branch bifurcates first and acquires stability at a saddle-node bifurcation before losing it again at larger amplitude at a symmetry-breaking steady state bifurcation. The P_+ branch is never stable, and neither are the mixed modes connecting the pure mode branches. Thus interesting behavior sets in beyond the symmetry-breaking bifurcation on the P_- branch, i.e., for $\mu > \mu_{SB} \approx 2.8$. In the following we describe the results of numerical integration of Eqs. (1)–(3) in this regime.

Once P_- loses stability at SB small perturbations drive the system to a stable branch of $R_1 R_2$-symmetric *periodic orbits*, also shown in Fig. 2. If the corresponding branch is continued backwards (i.e., for $\mu < \mu_{SB}$) one finds that it ultimately terminates in a heteroclinic bifurcation involving the nonsymmetric fixed points M. The eigenvalues of M at this bifurcation are 0.001940, -0.42229, $-0.998 \pm 4.819i$ and -1.58926 and hence no chaotic dynamics result. An entirely different scenario unfolds when this periodic branch is continued for $\mu > \mu_{SB}$. First, the $R_1 R_2$-symmetric branch undergoes a pitchfork bifurcation that generates a pair

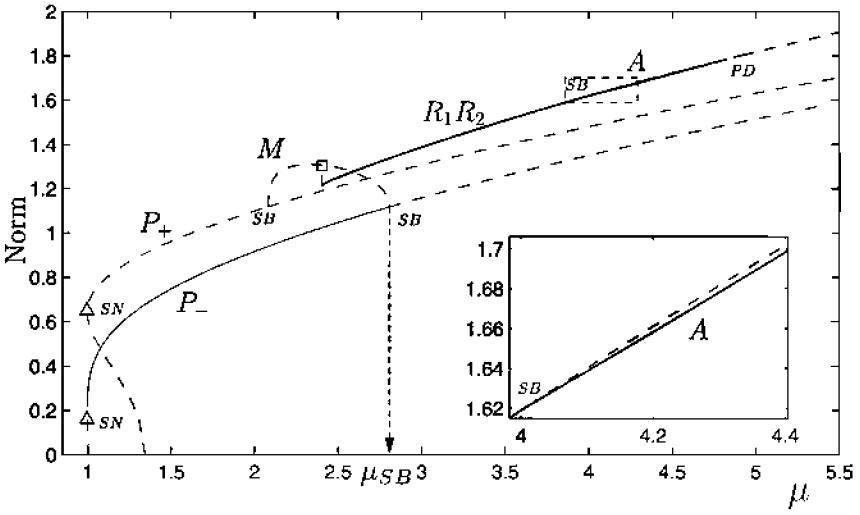

Fig. 2. Bifurcation diagram showing the (maximum) value of $||X+Y||$ as a function of μ. Thick solid (dashed) lines correspond to stable (unstable) periodic orbits; thin solid (dashed) lines correspond to stable (unstable) steady states. The arrow indicates the location of a subcritical bifurcation on P_- to unstable M. This bifurcation produces a hysteretic transition to stable R_1R_2-symmetric oscillations that exist between the heteroclinic bifurcation indicated by the symbol □ and a symmetry-breaking bifurcation labelled SB (inset)

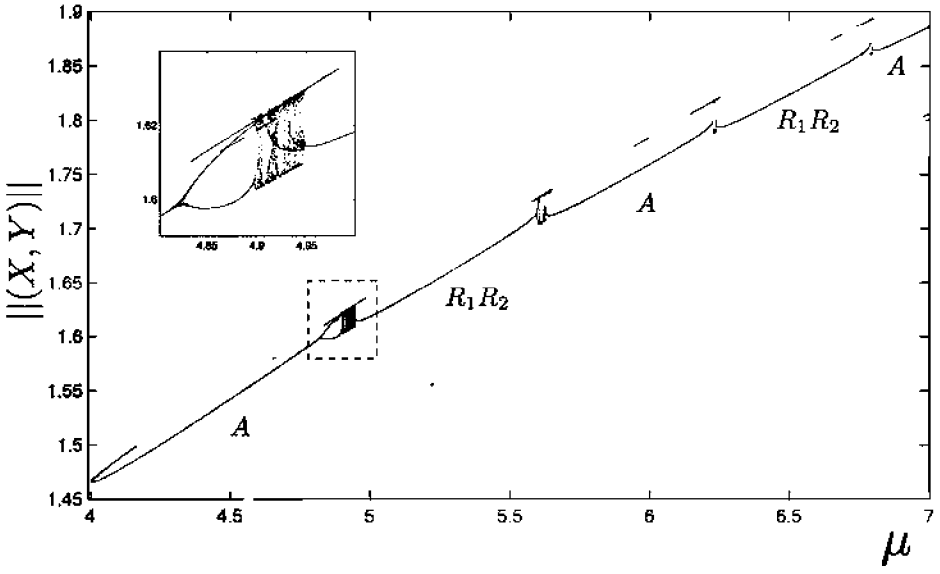

Fig. 3. Bifurcation diagram showing an alternating sequence of R_1R_2-symmetric (R_1R_2) and asymmetric (A) periodic orbits. The figure is constructed by recording successive maxima of $||(X,Y)|| \equiv \sqrt{||X||^2+||Y||^2}$ at each value of μ. The inset shows an enlargement of the first chaotic region

of stable asymmetric periodic orbits (see Fig. 2, inset). With a further increase in μ these asymmetric orbits undergo a period-doubling bifurcation PD and, as shown in the bifurcation diagram of Fig. 3, chaotic dynamics are found not long after. The chaotic behavior is marked by a *crisis* in which two asymmetric chaotic attractors collide at $\mu \approx 4.903$ and merge, forming a symmetric chaotic attractor (a symmetry-increasing bifurcation). The interval over which chaos is observed is relatively short ($4.902 \lesssim \mu \lesssim 4.92$), however, and the system is soon attracted to a new branch of R_1R_2-symmetric periodic orbits created in a saddle-node bifurcation. When, in turn, this R_1R_2-symmetric branch loses stability, we observe a new branch of stable asymmetric periodic orbits created in a nearby saddle-node bifurcation. This sort of alternating transition between R_1R_2-symmetric and asymmetric oscillations is repeated again and again. Note also that the

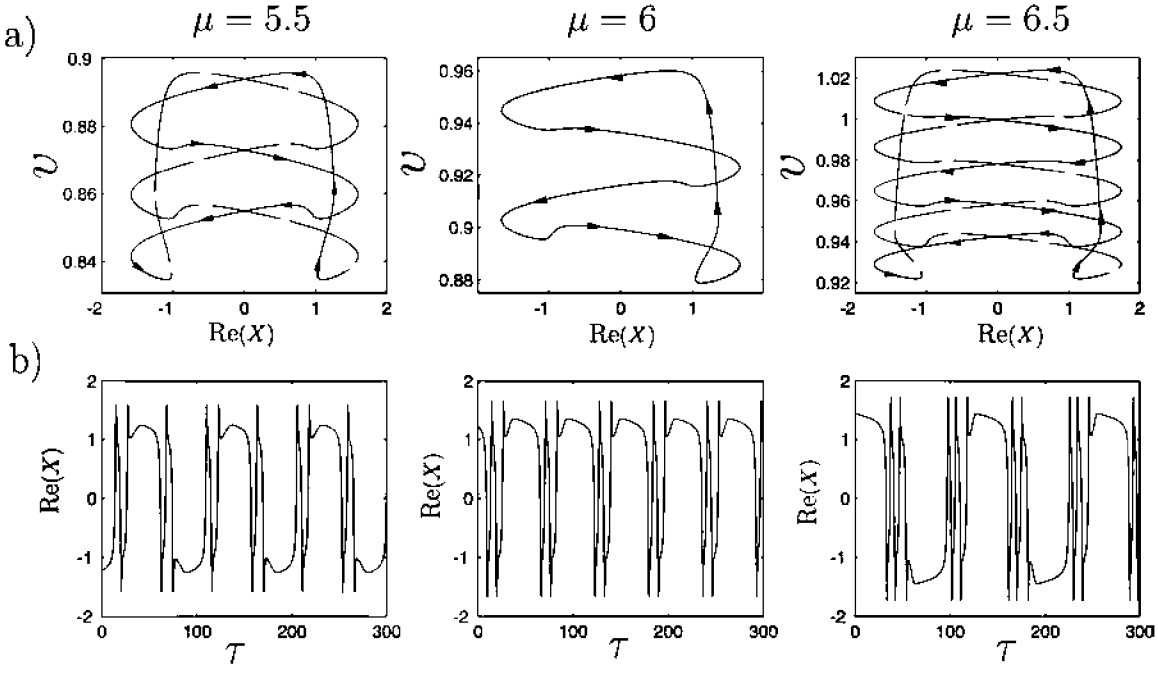

Fig. 4. (**a**) Projection onto the $(\mathrm{Re}(X), v)$ plane of stable symmetric and asymmetric periodic orbits in successive periodic windows in Fig. 3. (**b**) The corresponding time series $\mathrm{Re}(X(\tau))$

chaotic windows associated with these transitions become narrower and narrower as μ increases. In Fig. 4 we show stable attractors associated with three consecutive periodic windows in Fig. 3. These limit cycles are evidently *relaxation oscillations*, but of an unusual type, involving slow drifts along branches of both equilibria *and* of periodic orbits, with fast jumps between them. Moreover, these oscillations may be symmetric or asymmetric, with the symmetry alternately present and broken in successive periodic windows. In the following we suggest an explanation for this remarkable behavior.

To understand this behavior we rewrite Eqs. (1)–(3) in the form

$$\boldsymbol{X}' = \boldsymbol{F}_1(\boldsymbol{X}, \boldsymbol{Y}, v; \mu), \quad \boldsymbol{Y}' = \boldsymbol{F}_2(\boldsymbol{X}, \boldsymbol{Y}, v; \mu), \quad v' = \varepsilon G(\boldsymbol{X}, \boldsymbol{Y}, v), \tag{5}$$

where $\boldsymbol{X} = (\mathrm{Re}(X), \mathrm{Im}(X))$, $\boldsymbol{Y} = (\mathrm{Re}(Y), \mathrm{Im}(Y))$, and assume that $0 < \varepsilon \ll 1$. The properties of the relaxation oscillations can be understood by taking first the case of $\varepsilon = 0$. In this case v becomes a parameter, and Eq. (5) become

$$\boldsymbol{X}' = \boldsymbol{F}_1(\boldsymbol{X}, \boldsymbol{Y}; v, \mu), \quad \boldsymbol{Y}' = \boldsymbol{F}_2(\boldsymbol{X}, \boldsymbol{Y}; v, \mu). \tag{6}$$

This pair of equations can have both steady state solutions and periodic solutions. Of particular significance is the one-dimensional nullcline $\Sigma : \boldsymbol{F}_1(\boldsymbol{X}, \boldsymbol{Y}, v; \mu) = \boldsymbol{F}_2(\boldsymbol{X}, \boldsymbol{Y}, v; \mu) = 0$ that contains the steady states when $\varepsilon > 0$ and consists of them when $\varepsilon = 0$. As indicated in Fig. 5 the projection of Σ onto the $(v, \mathrm{Re}(X))$ plane consists of pairs of branches of stable ($S^{\pm}$) and unstable ($U^{\pm}$) states, related by symmetry. In addition to these branches of steady states Eq. (5) with $\varepsilon = 0$ also contain a one parameter family of attracting *limit cycles*. These periodic solutions are created, as v increases, in a heteroclinic bifurcation involving the two fixed points U^+ and U^-, and are $R_1 R_2$-symmetric. Between this heteroclinic bifurcation and the turning points $q^{\pm}$ the stable $R_1 R_2$-symmetric limit cycles coexist with the stable fixed points $S^{\pm}$ (see Fig. 5). When ε is finite but small these states couple to the slow evolution of the variable v, and the manifolds of steady states and periodic orbits become part of the *slow manifold* of the system (5). In the following we speak of the solutions as drifting along this manifold (the slow phase); this drift proceeds until the system is forced away from the slow manifold, heralding the onset of the fast phase of the oscillation that takes it back to the slow manifold. The plots in Fig. 4 can be interpreted in this manner, with episodes of almost constant $\mathrm{Re}(X)$ corresponding

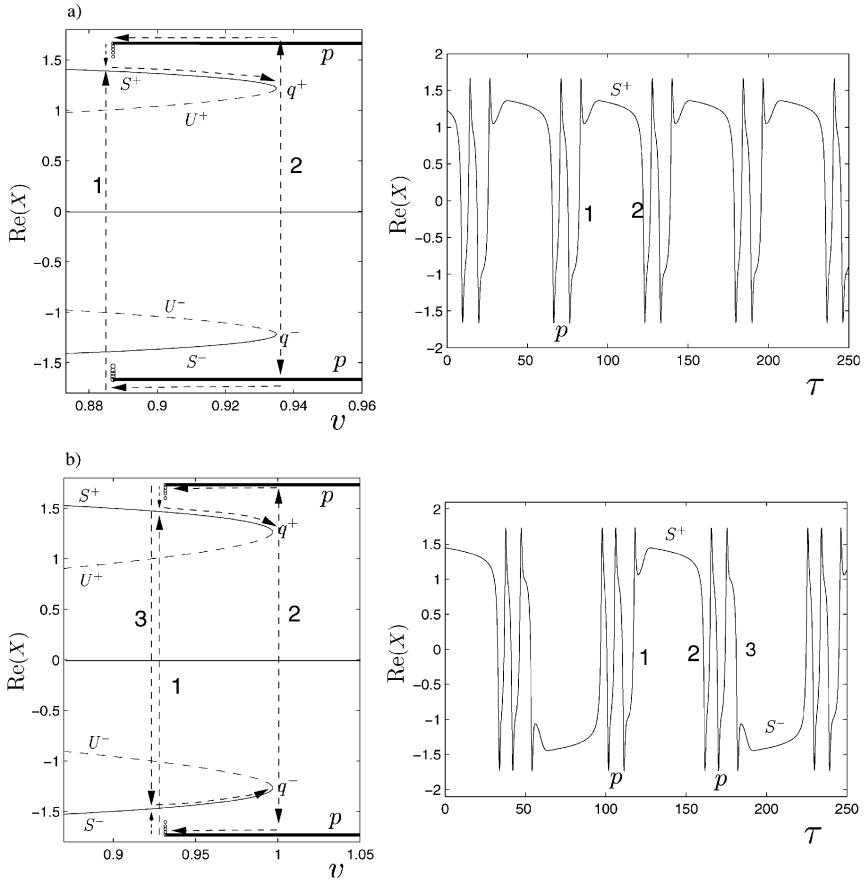

Fig. 5a,b. The slow manifold for system (5) lies within $O(\varepsilon)$ of the manifolds $S^{\pm}$, $U^{\pm}$ of steady states and the manifold p of periodic orbits of (5) with $\varepsilon = 0$. The slow drifts in v that occur when $0 < \varepsilon \ll 1$ are indicated by broken 'horizontal' arrows; the fast phase results in 'vertical' jumps. These are indicated by vertical arrows, and labelled by integers to indicate the corresponding transition in the associated time series $\mathrm{Re}(X(\tau))$. (**a**) Asymmetric relaxation oscillations of Eq. (5) when $\mu = 6.0$ and $\varepsilon = 0.01$. (**b**) R_1R_2-symmetric relaxation oscillations of Eq. (5) when $\mu = 6.5$ and $\varepsilon = 0.01$

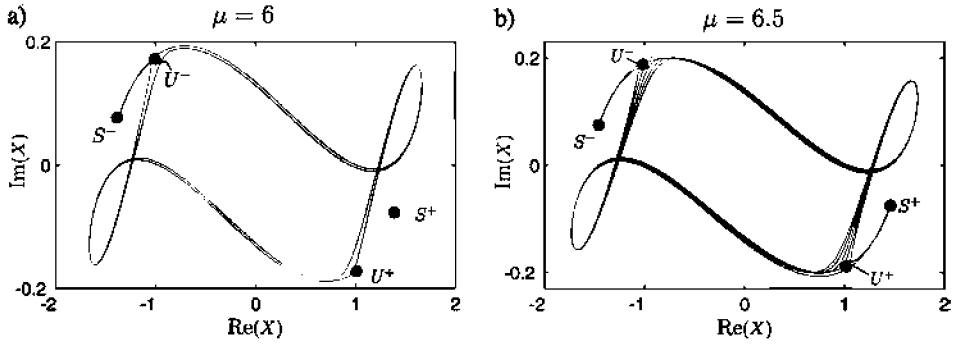

Fig. 6a,b. Projections of (**a**) an asymmetric solution at $\mu = 6.0$ and (**b**) an R_1R_2-symmetric solution at $\mu = 6.5$ on the $(\mathrm{Re}(X), \mathrm{Im}(X))$ plane, both calculated with $\varepsilon = 0.01$, showing the role played by the stable manifold of $U^{\pm}$ in determining the part of the slow stable manifold followed by the solution. The actual trajectory *spirals* around this manifold

to drift along the manifold of steady states $S^{\pm}$ with the return trajectory consisting of a drift along the branch of periodic orbits.

To understand the nature of the resulting relaxation oscillations in greater detail we begin by considering the drift along M_S^+, the part of the slow manifold near the stable steady states S^+. The drift is in the direction

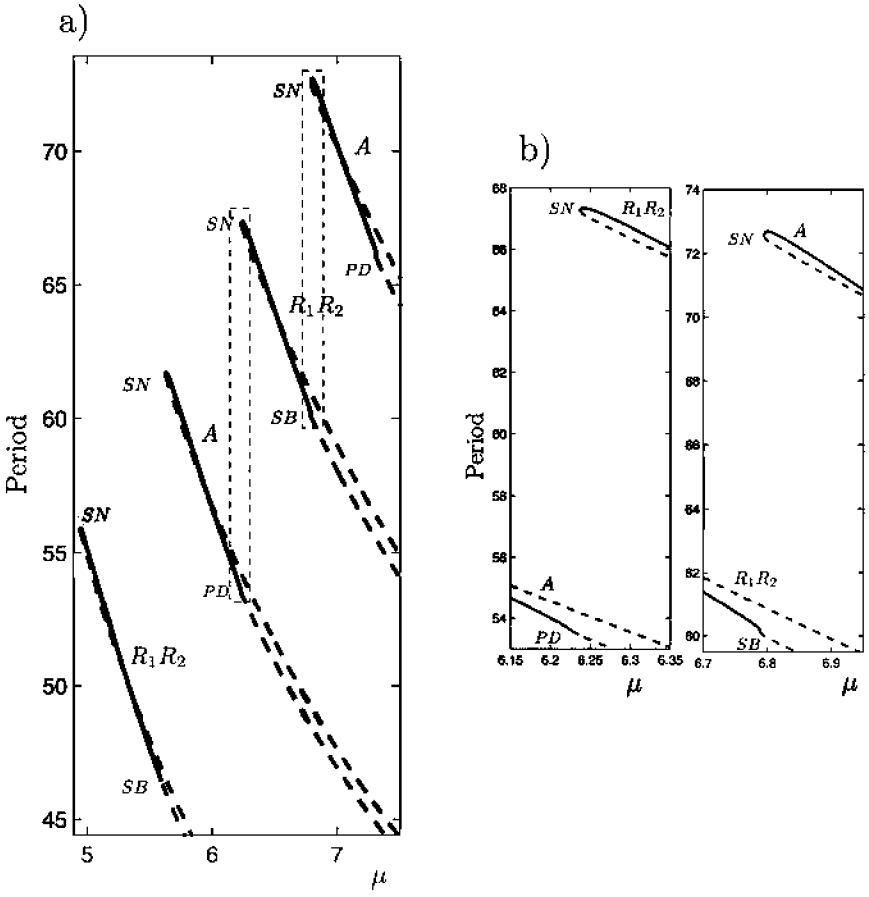

Fig. 7. Alternating sequence of R_1R_2-symmetric and asymmetric relaxation oscillations. The diagram shows the period (half-period) of asymmetric (symmetric) periodic relaxation oscillations as a function of μ. The solid (dashed) lines correspond to stable (unstable) states. The labels *SN*, *SB*, and *PD* denote saddle-node, symmetry-breaking and period-doubling bifurcations, respectively

of increasing v and so takes the system towards q^+ (see Fig. 5). Near this point this slow drift ends and the system jumps abruptly to the branch of symmetric periodic states, labelled p. In Fig. 5 this transition is indicated by a vertical short-dashed line, and labelled with the number 2. The system then drifts towards the left along the corresponding slow manifold M_p until it reaches the vicinity of the heteroclinic bifurcation where the oscillations disappear ($\varepsilon = 0$), and so does the associated slow manifold M_p ($0 < \varepsilon \ll 1$). With the disappearance of M_p the system is forced to either jump toward S^+ or toward S^-. Which of these two outcomes takes place is determined by the phase of the trajectory near U^+ or U^-. These states are saddles with one unstable direction and three stable directions. In what follows it is important that the least stable eigenvalue is in fact complex. For example, when $\varepsilon = 0$ the eigenvalues of $U^\pm$ at $\mu = 6.5$ are 0.6547, $-0.9999 \pm 14.236i$ and -2.65405, and these values are typical of the other periodic windows as well. The time series show clearly that when the drift along M_p ends the system approaches either U^+ or U^- along its stable manifold; what happens thereafter depends on which part of its unstable manifold is followed. If the unstable manifold of U^+, for example, takes the system to S^+ (as in Fig. 5a) the fast phase (labelled 1) terminates on S^+ and the system thereafter drifts towards the right along M_S^+. The resulting oscillation is an asymmetric relaxation oscillation. In contrast, if the unstable manifold of U^+ takes the system to S^- the fast phase terminates on S^- and the system thereafter drifts towards the right along M_S^-. In Fig. 5b this transition is labelled 3; the accompanying panel shows the corresponding signature in the time series. When the slow phase terminates the system jumps back to the large amplitude periodic state (transition 2) and drifts along it to the left, but this time when it falls off M_p in the transition labelled 1 it goes to U^- and by symmetry follows *its* unstable manifold towards S^+. The resulting trajectory is R_1R_2-symmetric. It is clear that these two outcomes are the

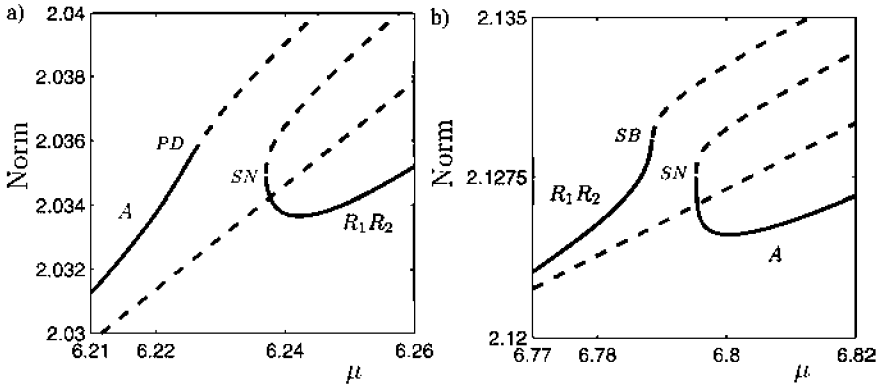

Fig. 8a,b. Detail of the bifurcation diagrams near the transition from asymmetric to symmetric relaxation oscillations near (**a**) $\mu = 6.23$, and (**b**) $\mu = 6.79$. Solid (broken) lines indicate stable (unstable) solutions. The labels *SN*, *SB*, and *PD* denote saddle-node, symmetry-breaking and period-doubling bifurcations, respectively

result of a π phase change in the direction in which the trajectory enters the neighborhood of U^+. Figure 6 shows the oscillations of Fig. 4 in a projection that highlights the role of the stable manifold of these unstable steady states as a separatrix between the two slow phases of the relaxation oscillation.

The above discussion points to a very specific role of the *unstable* steady states $U^{\pm}$ in determining whether the oscillations are symmetric or asymmetric. This is because, as already mentioned, the periodic states p disappear in a heteroclinic connection involving these two states; this in turn is a consequence of the R_1R_2 symmetry of the p states. Consequently it comes as no surprise that these steady states are involved in the transition from one type of oscillation to the other, and in the associated windows of chaos (see Fig. 3). To understand the main features revealed in Fig. 3 we examine the period along the successive branches of periodic oscillations as μ increases. We find that as μ increases each periodic oscillation is born in a saddle-node bifurcation, and that the period decreases along both the stable and the unstable branches away from these saddle-node bifurcations (see Fig. 7). In each case the long period appears to be related to the close approach of the trajectory to one of the unstable steady states $U^{\pm}$ although no global bifurcation takes place. Figure 8 shows what happens in a bifurcation diagram, and highlights the sequence of bifurcations that occur in every transition from an asymmetric oscillation to a symmetric one, and from a symmetric one to an asymmetric one. Figure 9 looks at one of these in more detail. This figure focuses on the branch of asymmetric relaxation oscillations that first appears in a saddle-node bifurcation near $\mu = 7.0$. Figure 9b shows that many of the characteristic features of the time series are related to the approach of the trajectory to the unstable steady states $U^{\pm}$. Moreover, the figure also shows that as one follows the stable branch from the saddle-node towards larger μ one encounters an interval of μ in which the period drops precipitously (Fig. 9a, inset), behavior that is a consequence of the trajectory switching from the slow stable manifold $S^{\pm}$ to the slow unstable manifold $U^{\pm}$. Just after this point the stable (asymmetric) relaxation oscillation loses stability via period-doubling; this period-doubled oscillation is not shown. Figure 9b shows the time series at the point marked 3 ($\mu \approx 7.31$) just before this loss of stability, and reveals that the trajectory reverts back to $S^{\pm}$ before the fast transition to the oscillatory phase. However, as μ increases the trajectory starts to follow the unstable manifold all the way to the saddle-node at q^- (see point marked 5, $\mu \approx 7.5$) and the resulting relaxation oscillation is unstable. For larger μ the oscillation remains unstable but the trajectory departs from U^- in the *opposite* direction (see point marked 6, $\mu \approx 10$). The observed behavior appears to be a consequence of the fact that the leading stable (i.e., the least stable) eigenvalues λ_s of $U^{\pm}$ are *complex*. It follows that when the R_1R_2-symmetric oscillations collide with $U^{\pm}$ at the heteroclinic bifurcation, present when $\varepsilon = 0$, the trajectory approaches both these steady states in the form of a spiral, before leaving along the unstable manifold. The corresponding unstable eigenvalue $\lambda_u < |\mathrm{Re}(\lambda_s)|$, precluding chaotic dynamics in the $\varepsilon = 0$ system. When $0 < \varepsilon \ll 1$ this type of motion persists but is now accompanied by a slow drift along the slow manifold M_p towards the region of the $\varepsilon = 0$ heteroclinic bifurcation. The situation where $\lambda_u > |\mathrm{Re}(\lambda_s)|$ in the fast system ($\varepsilon = 0$) is also of interest, although it does not occur for the parameter values explored here.

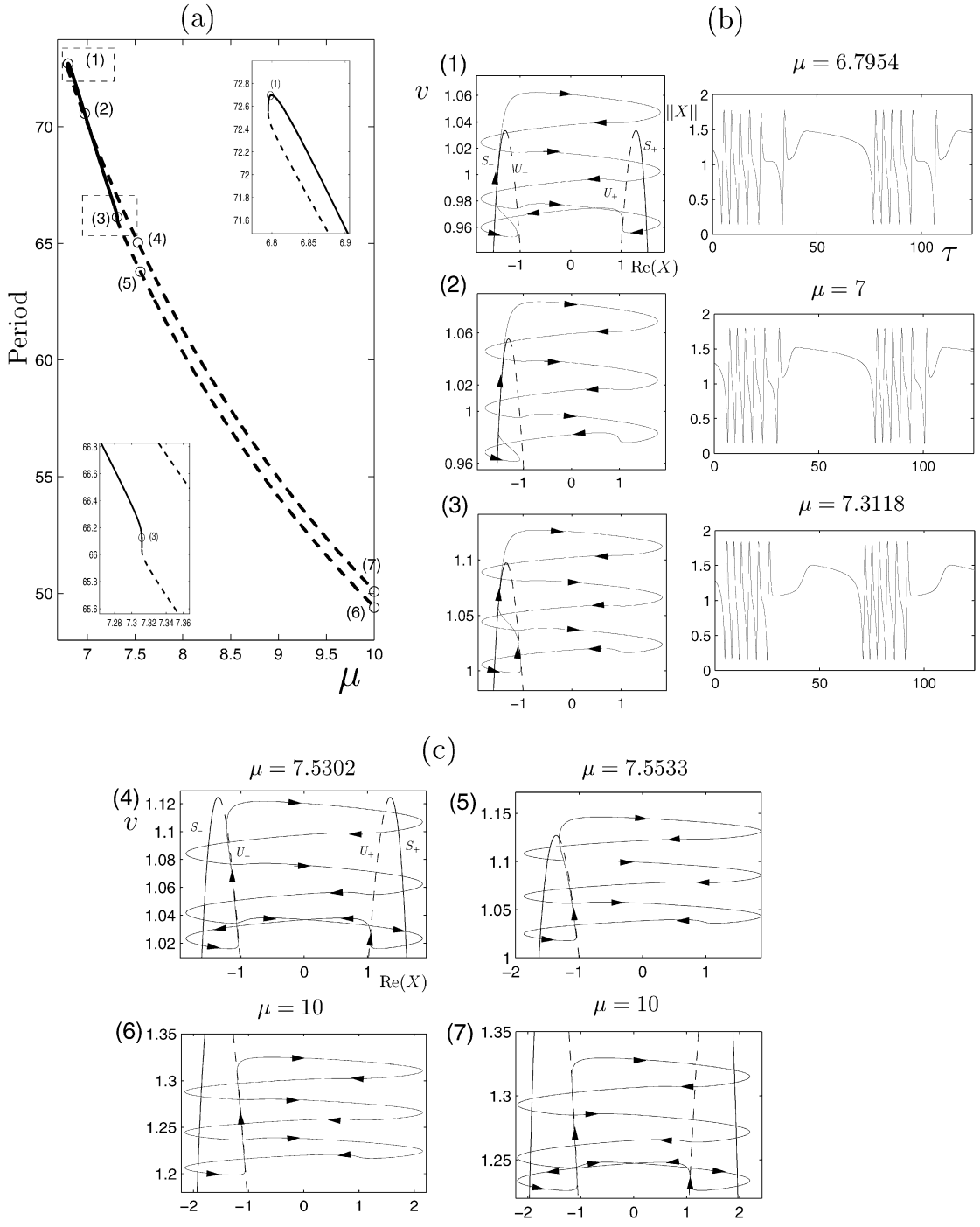

Fig. 9. (**a**) Period of asymmetric relaxation oscillations as a function of μ. Solid (dashed) lines correspond to stable (unstable) states. (**b**) Stable relaxation oscillations corresponding to the open circles (1,2,3) in figure (**a**) projected on the (Re(X), v) plane together with the corresponding time series $||X(\tau)||$. (**c**) Unstable relaxation oscillations corresponding to the remaining open circles (4,5,6,7) in figure (**a**) in the same projection

In Fig. 10 we summarize the corresponding results for $\varepsilon = 0.01$ and $\mu = 9.0$ using the norm $||(X, Y)|| \equiv \sqrt{||X||^2 + ||Y||^2}$ to indicate the oscillation amplitude, cf. Fig. 5. We see that the oscillations terminate in a heteroclinic bifurcation involving the unstable states $U^{\pm}$. During one part of the slow phase (labelled 1) the system drifts towards smaller v along the slow manifold M_p of stable periodic solutions p. When it reaches

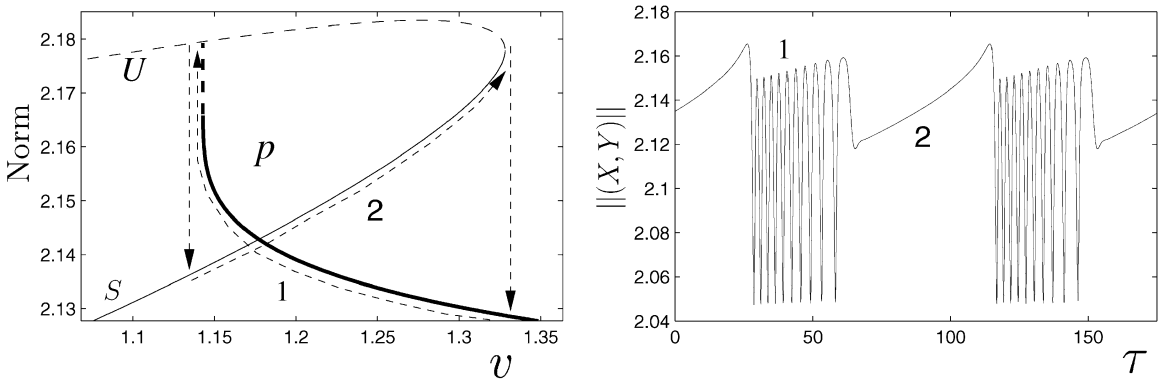

Fig. 10. Slow manifold for the system (5) consisting of stable periodic orbits (solid line) and stable steady states (thin line) of Eq. (5) with $\varepsilon = 0$ and $\mu = 9.0$. The slow drifts, present when $0 < \varepsilon \ll 1$, are labelled with numbers to indicate the corresponding phase in the accompanying time series $||(X, Y)||$, computed from Eq. (5) with $\varepsilon = 0.01$ and $\mu = 9.0$. The arrows indicate the direction of drift as well as the fast transitions. The relaxation oscillations are asymmetric

the location of the global bifurcation the oscillations end, and the system undergoes a rapid transition to a stable state S indicated by a vertical arrow. Thereafter it enters a new slow phase, labelled 2, and drifts in the direction of increasing v, towards the turning point q, where the slow phase ends and the system makes a rapid transition back to M_p. This transition is also indicated by a vertical arrow. The resulting time series is quite dramatic (Fig. 10) and reveals the two slow phases very clearly, as well as the rapid transition between them. In fact one can verify that the small cusp-like feature just prior to the onset of phase 2 is due to the spiraling of the trajectory towards the unstable steady state U before being ejected along the unstable manifold of U.

Except for the presence of the oscillatory slow phase the time series in Fig. 10 corresponds to a standard relaxation oscillation. Similar relaxation oscillations are associated with the higher saddle-node bifurcations as well (cf. Fig. 7). However, in appropriate albeit small ranges of μ the oscillations take on a new form, and exhibit canard-like behavior (Fig. 11): the slow phase now includes a drift along part of the *unstable* slow manifold M_U. This drift is quite clearly visible in the corresponding time series. Notice that both solutions shown in Fig. 11 are periodic and stable, and are computed for almost identical values of the parameter μ, and yet are very different. In Fig. 11a the system drops to the unstable steady state at the end of the slow phase 1, and then drifts along M_U (labelled 2 in Fig. 11a) towards larger v before a sudden jump to M_S. The slow drift (labelled 3) continues along M_S towards the turning point on Σ where the system jumps to the oscillatory state p, and the slow phase 1 recommences. In contrast, the solution in Fig. 11b jumps from M_U to M_p (instead of M_S) and so begins to drift towards smaller v but the next time, instead of following M_U, it jumps to M_S and begins to follow the standard relaxation oscillation scenario. As already mentioned, the resulting difference in the time series is dramatic. The extreme sensitivity of these solutions to the precise value of μ is an indication that this is indeed a canard, but this time it is evidently associated with the slow passage through the global bifurcation with which the periodic states p terminate on U. We emphasize that these relaxation oscillations, like those in Fig. 9, vary a great deal along each of the oscillatory branches created in the original saddle-node bifurcation, but that away from the canard-like behavior just described, this variation is gradual and occurs over $O(1)$ intervals in μ.

Finally, it is also clear that with each half-turn of the trajectory around $U^{\pm}$ the trajectory will change the direction in which it leaves $U^{\pm}$. When the number of turns increases monotonically with μ there will be an infinite sequence of symmetry-changing transitions, and hence a sequence of periodic windows with alternating symmetric and asymmetric relaxation oscillations. Moreover, since it takes a finite interval in μ to change the frequency sufficiently to add a half-turn these symmetry-changing transitions cannot accumulate, in contrast to the cascades of symmetry-switching gluing bifurcations that occur in other D_2-symmetric systems [5].

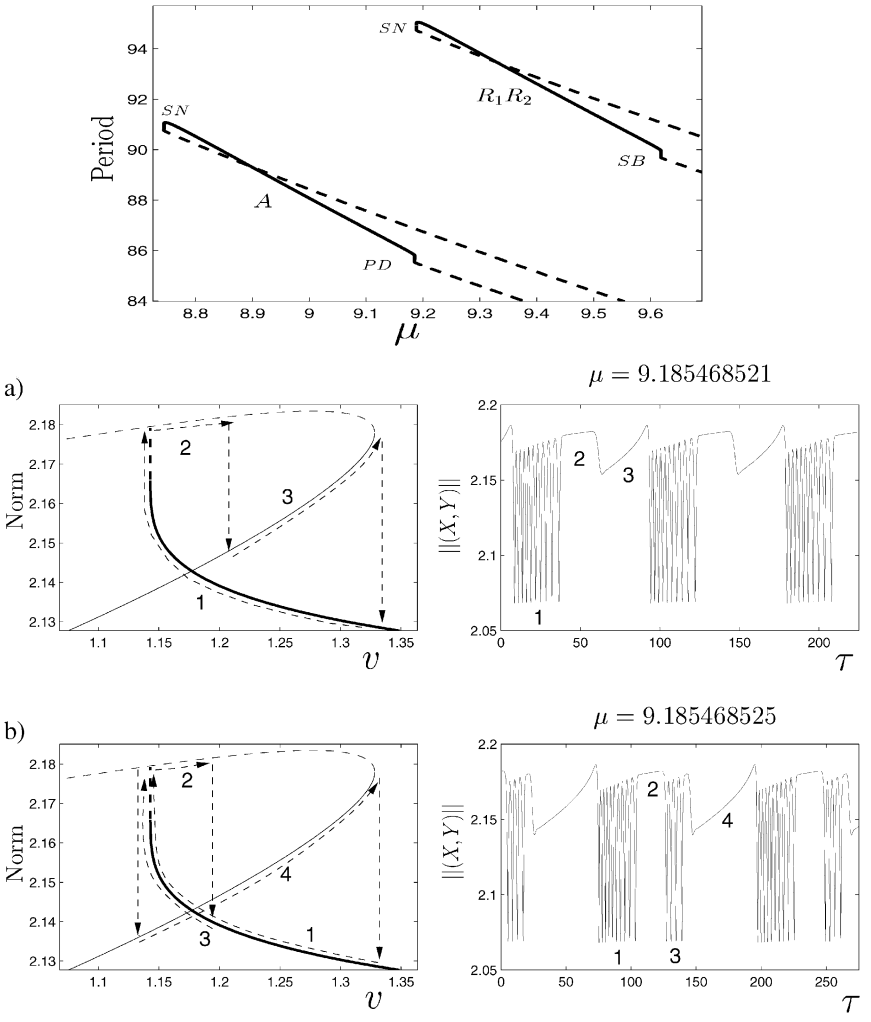

Fig. 11a,b. As in Fig. 10, but for (**a**) $\mu = 9.185468521$ and (**b**) $\mu = 9.185468525$, showing stable relaxation oscillations exhibiting canard-like behavior. The top panel shows the location of these solutions in a period vs μ plot (Fig. 7). The slow drifts, present when $0 < \varepsilon \ll 1$, are labelled with numbers to indicate the corresponding phase in the accompanying time series $||(X, Y)||$, computed from Eq. (5) with $\varepsilon = 0.01$. The arrows indicate the direction of drift as well as the fast transitions. In all three cases the relaxation oscillations are asymmetric

2 Discussion

In this paper we have examined the dynamics of parametrically driven Faraday waves in slightly elliptical containers on the assumption that (i) the viscosity of the liquid is small (as measured by the dimensionless quantity $C_g \ll 1$) and (ii) the effective Reynolds number of the streaming flow driven in oscillatory boundary layers is also small. Under these conditions the system is described by a five-dimensional system of ordinary differential equations. The eccentricity of the container, although small, is of crucial importance in the phenomena identified here since it results in a coupling of the streaming flow to the complex amplitudes of the two nearly degenerate modes. As in other problems of this type [11], such an interaction often leads to complex dynamics. We have seen that when ε is small (i.e., the streaming flow is weakly damped) relaxation oscillations may result. These are oscillations consisting of slow phases interrupted by fast 'jumps' from one state to another. A particularly novel property of our system is the presence of jumps between steady and periodic states. In the Faraday system the periodic oscillations correspond to mixed mode oscillations in which the contribution of the two orthogonal standing waves oscillates periodically in time (as does their relative phase), and the relaxation oscillations found are oscillations between this complex state and a standing wave. However, the basic picture is quite simple: the system drifts along the slow manifold until it passes a bifurca-

tion, typically a saddle-node bifurcation although in our case a global bifurcation plays a similar role, where it is forced away from the slow manifold. The resulting fast phase then takes it to another part of the slow manifold and the process repeats. The resulting time series (Fig. 10) appear indistinguishable from the type of (so-called parabolic) bursting behavior exhibited by neurons [13]. In our system we have seen that oscillations of this type occur when the streaming flow is weakly damped. As a result, the streaming flow behaves as a slowly varying parameter, and the system drifts along the slow manifold computed by 'freezing' the mean flow.

Because of the D_2 symmetry of our equations additional phenomena occur. We have seen that as μ increases there is an infinite sequence of transitions between asymmetric and $R_1 R_2$-symmetric oscillations, each associated with a narrow interval of chaotic dynamics. These transitions are hysteretic, and involve canard-like behavior, associated with the passage of the system through a global (in our case, heteroclinic) bifurcation in the fast system, cf. [1, 3, 4]. In addition we saw that the change of symmetry between successive periodic windows is due to an extra half-turn of the trajectory around the unstable steady states as μ increases. This point of view allowed us to understand why the intervening chaotic intervals become narrower with increasing μ but the 'symmetry-switching' transitions do not accumulate at a finite value of μ. The presence of relaxation oscillations, let alone of canards, is unusual in fluid dynamics, and we believe that our study represents the first time that ducks have been found in water. A forthcoming paper describes our results in greater detail [6].

Acknowledgments. This work was supported in part by EPSRC grant GR/R52879/01 and by an EPSRC visitor grant at Leeds University (MH). We are grateful to Drs. J. Moehlis and J. Porter for numerous discussions.

References

1. Arnol'd, V.I., Afrajmovich, V.S., Il'yashenko, Yu.S., Shil'nikov, L.P.: Bifurcation Theory and Catastrophe Theory. In *Encyclopaedia of Mathematical Sciences*, Vol. 5, V.I. Arnol'd (ed.), Springer-Verlag, NY (1994)
2. Douady, S., Fauve, S., Thual, O.: Oscillatory phase modulation of parametrically forced surface waves. Europhys. Lett. **10**, 309–315 (1989)
3. Eckhaus, W.: Relaxation oscillations, including a standard chase on french ducks. *Lecture Notes in Mathematics*, 985, pp. 449–494, Springer-Verlag, NY (1983)
4. Guckenheimer, J., Hoffman, K., Weckesser, W.: Numerical computation of canards. Int. J. Bif. Chaos **10**, 2669–2687 (2000)
5. Higuera, M., Porter, J., Knobloch, E.: Heteroclinic dynamics in the nonlocal parametrically driven nonlinear Schrödinger equation. Physica D **162**, 155–187 (2002)
6. Higuera, M., Knobloch, E., Vega, J.M.: Dynamics of nearly inviscid Faraday waves in almost circular containers. Physica D, submitted
7. Higuera, M., Vega, J.M., Knobloch, E.: Coupled amplitude-streaming flow equations for nearly inviscid Faraday waves in small aspect ratio containers. J. Nonlin. Sci. **12**, 505–551 (2002)
8. Martel, C., Nicolás, J.A., Vega, J.M.: Surface-wave damping in a brimful circular cylinder. J. Fluid Mech. **360**, 213–228 (1998). See also Corrigendum **373**, 379 (1998)
9. Martín, E., Martel, C., Vega, J.M.: Drift instability of standing Faraday waves. J. Fluid Mech. **467**, 57–79 (2002)
10. Miles, J.W.: Internally resonant surface waves in a circular cylinder. J. Fluid Mech. **149**, 1–14 (1984)
11. Moehlis, J., Knobloch, E.: Forced symmetry breaking as a mechanism for bursting. Phys. Rev. Lett. **80**, 5329–5332 (1998)
12. Vega, J.M., Knobloch, E., Martel, C.: Nearly inviscid Faraday waves in annular containers of moderately large aspect ratio. Physica D **154**, 313–336 (2001)
13. Wang, X.J., Rinzel, J.: Oscillatory and bursting properties of neurons. In *Brain Theory and Neural Networks*. M.A. Arbib (ed.), MIT Press: Cambridge, MA (1995)